

Lensless digital holographic microscopy and its applications in biomedicine and environmental monitoring



Yichen Wu^{a,b,c}, Aydogan Ozcan^{a,b,c,d,*}

^a Electrical Engineering Department, University of California, Los Angeles, CA 90095, USA

^b Bioengineering Department, University of California, Los Angeles, CA 90095, USA

^c California NanoSystems Institute (CNSI), University of California, Los Angeles, CA 90095, USA

^d David Geffen School of Medicine, University of California, Los Angeles, CA 90095, USA

ARTICLE INFO

Article history:

Received 30 July 2017

Received in revised form 23 August 2017

Accepted 24 August 2017

Available online 31 August 2017

ABSTRACT

Optical compound microscope has been a major tool in biomedical imaging for centuries. Its performance relies on relatively complicated, bulky and expensive lenses and alignment mechanics. In contrast, the lensless microscope digitally reconstructs microscopic images of specimens without using any lenses, as a result of which it can be made much smaller, lighter and lower-cost. Furthermore, the limited space-bandwidth product of objective lenses in a conventional microscope can be significantly surpassed by a lensless microscope. Such lensless imaging designs have enabled high-resolution and high-throughput imaging of specimens using compact, portable and cost-effective devices to potentially address various point-of-care, global-health and telemedicine related challenges. In this review, we discuss the operation principles and the methods behind lensless digital holographic on-chip microscopy. We also go over various applications that are enabled by cost-effective and compact implementations of lensless microscopy, including some recent work on air quality monitoring, which utilized machine learning for high-throughput and accurate quantification of particulate matter in air. Finally, we conclude with a brief future outlook of this computational imaging technology.

© 2017 Elsevier Inc. All rights reserved.

Contents

1. Introduction	5
2. Lensless holographic microscope on a chip	5
2.1. Theory and design principles	5
2.2. Pixel super-resolution for on-chip holographic imaging	7
2.3. Illumination angle diversity for enhanced resolution: synthetic aperture microscopy	8
2.4. Digital hologram reconstruction	8
2.5. Phase-retrieval using multi-height measurements	9
2.6. Compressive sensing/sampling and sparsity based phase retrieval	10
2.7. Phase retrieval using deep-learning	10
2.8. Color imaging in lensless digital holographic microscopy	11
2.9. Lensless 3D imaging and tomography on a chip	11
2.10. Nano-particle detection and sizing using lensless on-chip microscopy	11
3. Air quality monitoring using digital holography on a chip	12
3.1. c-Air: a hand-held, accurate, cost-effective and high-throughput PM monitor based on machine learning	12
4. Outlook	13
Acknowledgements	13
References	14

* Corresponding author at: 420 Westwood Plaza, Engr. IV 68-119, UCLA, Los Angeles, CA 90095, USA.

E-mail address: ozcan@ucla.edu (A. Ozcan).

1. Introduction

For centuries, biomedical imaging at micron-scale has been powered by optical compound microscopes, leading to numerous discoveries at the micro- and nano-scale [1,2]. These conventional microscopes are operated with relatively expensive and bulky lenses and other opto-mechanical parts, including alignment mechanics, which altogether make the imaging system hard to operate in field settings. Furthermore, there is an inherent trade-off between the resolution and field-of-view (FOV) in a conventional microscope, where the resolution and field-of-view are coupled to each other. This means if we want to observe finer details with better resolution, we can only do so in a relatively smaller region of the sample using a single frame. Moreover, conventional lens-based optical microscopy also has limited depth-of-field (DOF), which makes it challenging to screen large volumes of samples.

Over the last few decades, as the computational resources have become exponentially faster, cheaper, more powerful and portable [3], unconventional microscopy methods have emerged that use very simple and inexpensive hardware while relying on computation to digitally generate high-resolution images over large sample areas and volumes [4–7]. Among these emerging computational microscopy techniques, lensless on-chip microscopy [8,9] has been extensively explored to by-pass various limitations of a conventional compound microscope, providing much more compact, cost-effective and wider FOV imagers.

In a lensless on-chip microscope (Fig. 1(a)), the sample is placed above an image sensor chip with a spacing of <1 mm, without any imaging lenses in between. A partially coherent light source illuminates the sample from the top. Instead of capturing a microscopic image of the sample directly, the image sensor records an in-line hologram [10] of the sample under partially coherent illumination. From this recorded hologram, the original object, both its amplitude and phase images, can be reconstructed digitally [8,10]. The absence of imaging lenses and alignment mechanics, and other bulky optical components, makes lensless on-chip microscopy extremely compact, cost-effective and light-weight. Moreover, the FOV and resolution are decoupled from each other: the resolution generally depends on the pixel size of the image sensor chip and the detection signal-to-noise ratio (SNR), whereas the sample FOV is equal to the entire active area of the sensor chip, which is

e.g., $20\text{--}30\text{ mm}^2$ for a state-of-the-art complementary metal oxide semiconductor (CMOS) imager chip and it can reach $\sim 10\text{--}20\text{ cm}^2$ for a Charge-Coupled-Device (CCD). These sample FOVs are orders of magnitude larger than the FOV of a conventional microscope (see Fig. 1(b) for a comparison). Furthermore, the holographic nature of lensless on-chip imaging enables three dimensional (3D) reconstruction of samples at extended DOF by digitally re-focusing to different reconstruction planes within a sample volume, assuming that the sample does not create dead spots due to optical shadowing. Numerous applications of lensless on-chip microscopy have been demonstrated so far, taking advantage of its compactness, cost-effectiveness and portability, including cancer and disease diagnosis [4,11,12], water-quality monitoring [13–15], microbial viability testing [16], 3D motion tracking of biological samples [17–20], analyzing high-energy particle tracks [21], among others [22,23].

In this manuscript, we review the basic design principles and the underlying computational algorithms for lensless digital holographic microscopy on a chip, also covering various applications that have been demonstrated using this imaging approach. Other lensless approaches that involve e.g., shadow imaging [24], plasmonic sensing [25–29] are beyond the scope of this review, which can be found in other reviews [2,30]. We will conclude by providing a future outlook of this computational imaging technology.

2. Lensless holographic microscope on a chip

2.1. Theory and design principles

In a lensless on-chip microscope, a semi-transparent sample is placed on top of an image sensor with a typical spacing of <1 mm (z_2 distance). A partially coherent light source is used as illumination, usually at $>2\text{--}3$ cm (z_1 distance) above the sample; as a result, the sample casts an in-line hologram, which is directly recorded by a CMOS or CCD image sensor, without using any imaging lenses. The light source can be either a monochromator [24,31] or a laser [4,32] in a benchtop system or a light emitting diode (LED) in a portable device [9,33], with an optional spectral filter (to fine tune the temporal coherence at the sensor plane) [34]. The benefits of a partially coherent source (both temporally and spatially), compared to its coherent counterpart (e.g., a laser

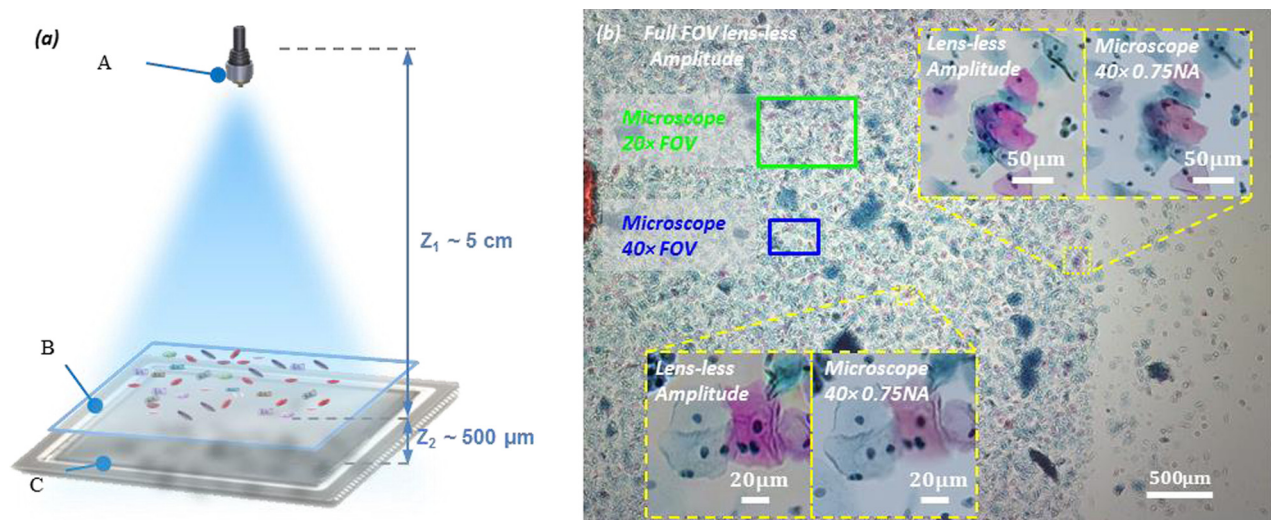


Fig. 1. Lensless holographic on-chip microscopy. (a) Schematics of a lensless on-chip microscope, including (A) a partially coherent light source (e.g., a multi-mode fiber-coupled LED), (B) the sample to be imaged (sample plane), and (C) image sensor chip (sensor plane). (b) Color reconstruction of a Pap smear. The reconstruction resolution and image quality are comparable to conventional microscope images, shown in the inset. The figure is modified from Ref. [93].

source) include reduced speckle and multiple reflection interference noise as well as much easier automated alignment of digital images for e.g., enhancement of lateral and axial resolution [8,35]. Unlike other digital holographic microscopes, an on-chip microscope does not need to use a small (e.g., sub-micron) pinhole since $z_1 \gg z_2$; in fact it can operate with very large apertures (e.g., 50–100 μm) without affecting its spatial resolution due to aperture induced smearing and coherence requirements – a detailed discussion of this can be found in the Appendix of Ref. [9]. Despite the use of partial spatial coherence, free space diffraction over a distance of $>2\text{--}3\text{ cm}$ (i.e., z_1 distance) creates sufficient coherence on the sample/sensor plane so that each individual point scatterer can be effectively considered coherent with respect to its local neighbors.

The hologram generated in a lensless digital holographic microscope is an in-line (Gabor) hologram [10]. In in-line holography, the object is semi-transparent and it can be approximated as:

$$t(x_0, y_0) = 1 + \Delta t(x_0, y_0) \quad (1)$$

where $\Delta t \ll 1$. When this object is locally illuminated by a plane wave A , it will propagate *coherently* over a distance of z_2 , where z_2 is the spacing between the sample and sensor planes:

$$\begin{aligned} R[z_2]\{A \cdot t(x_0, y_0)\} &= R[z_2]\{A\} + R[z_2]\{A \cdot \Delta t(x_0, y_0)\} \\ &= A' + a(x, y) \end{aligned} \quad (2)$$

where $R[z_2]\{\cdot\}$ is the free-space propagation operator over a depth of z_2 . Then at the sensor plane, a hologram is formed by the interference of the scattered sample beam $a(x, y)$ with the un-scattered reference beam A' , and the intensity of this interference is recorded by the sensor chip:

$$\begin{aligned} I(x, y) &= |A' + a(x, y)|^2 \\ &= |A'|^2 + A'^* \cdot a(x, y) + A' \cdot a^*(x, y) + |a(x, y)|^2 \end{aligned} \quad (3)$$

Because $z_1 \gg z_2$, the magnification of lensless microscopy is unit, meaning that the FOV is equal to the entire active area of the image sensor chip. In Eq. (3), the object related holographic information is encoded within the second and third terms, which are complex conjugates of each other. The first term can be subtracted out using a background image (without the object present), and the fourth term (i.e., $|a(x, y)|^2$) can be ignored since $\Delta t \ll 1$. In fact, this last term represents the self-interference of the scattered waves from the specimen, and does not contain any useful information as far as holography is concerned. This self-interference noise is suppressed by partial spatial and temporal coherence of the illumination, which can be considered as an “engineered coherence gate”. Simple back-propagation of Eq. (3), after the background subtraction, will result in both a focused image and a defocused image of the specimen that spatially overlap, and the latter forms what is commonly known as the twin-image artifact in in-line holography. Since z_2 is rather small for an on-chip microscope, this twin-image can strongly obscure the real object image, especially for connected and dense specimens, and in the next sub-sections we will discuss different strategies to suppress and eliminate twin image artifact in the reconstruction process.

There are several factors that can limit the resolution of a holographic on-chip microscope, which include e.g., diffraction, pixel size, image chip area and coherence of the system. Theoretically, if the pixel size can be arbitrarily small and the coherence is perfect over a large sensor area, then an image that is ideally reconstructed using a lensless on-chip microscope is diffraction limited, with a maximum detectable spatial frequency of $\sim n/\lambda$, where n is the refractive index of the medium between the sample and the sensor plane, and λ is the illumination wavelength.

In practice, an important limitation of the lensless on-chip microscope resolution is created by the pixel size of the sensor,

which is especially important due to its unit magnification. Practically, the half-pitch resolution of a reconstructed image using a state-of-art CMOS image sensor chip (such as the ones that are used in smart phone cameras) will be about one micron. With additional image processing, such as using pixel super-resolution algorithms, detailed in the next sub-section, an effective pixel size that is much smaller than the wavelength of light can be digitally synthesized from a series of low resolution measurements that are shifted with respect to each other.

The coherence of the illumination can be another source of resolution limitation due to partial spatial coherence and/or temporal coherence. In a lensless on-chip holographic microscope, the spatial coherence diameter at the sample plane is proportional to $\lambda \cdot z_1/D$, where D is the aperture size at the illumination plane, which can be a simple pinhole or a multi-mode fiber. For a given λ and z_1 , the choice of D affects not only the diameter of the spatial coherence at the sensor plane (which determines the effective numerical aperture in an object's in-line hologram) but also the spatial smearing that is induced at the hologram plane. To expand on the latter point, a given illumination aperture, $T(x, y)$, effectively smears the hologram intensity that is measured [9,36], i.e.,

$$I^{meas} = I^{coh} \star T\left(-\frac{z_1}{z_2}x, -\frac{z_1}{z_2}y\right) \quad (4)$$

where I^{coh} is the hologram assuming perfect spatial coherence over a large image sensor area (e.g., using an infinitesimally small pinhole), and I^{meas} is the measured hologram, and \star stands for the spatial convolution operation. Eq. (4) states that the aperture function is de-magnified by a factor of $M = z_1/z_2$ and projected onto the hologram plane. Intuitively, this convolution relation of Eq. (4) can be thought as an incoherent super-position of an infinite number of holograms, each of which is generated by an infinitesimal point source inside the aperture region, and assuming a perfectly incoherent illumination source across $T(x, y)$, each one of these point sources is incoherent with respect to others. To avoid this resolution limit due to pinhole or illumination aperture size, the projected/de-magnified aperture needs to be smaller than the pixel size so that the projected aperture equivalently merges into the pixel function. For an on-chip holographic microscope, this is easy to satisfy since $M = \frac{z_1}{z_2} \gg 1$; for example, for an aperture diameter of 100 μm , and a z_2 distance of 400 μm , a z_1 distance of $>3\text{--}4\text{ cm}$ should be sufficient for a typical CMOS imager chip that has a pixel size of $\sim 1\text{--}2\text{ }\mu\text{m}$.

The temporal coherence of the illumination is another factor that is crucial for the spatial resolution of an on-chip holographic microscope and is determined by the coherence length ΔL_c of (a single point) illumination source, which is a function of the spectral bandwidth $\Delta\lambda$ of the source [37]:

$$\Delta L_c \approx \left(\frac{2 \ln 2}{\pi}\right) \cdot \frac{\lambda^2}{n \cdot \Delta\lambda} \quad (5)$$

where n is refractive index, and λ is illumination wavelength. In order for a spatial frequency component of the object to be recorded at the sensor plane, the difference of the optical path-length of this high frequency scattered wave and the vertical reference wave should not exceed the temporal coherence length. Accordingly, the maximum angle (θ_{max}) for any scattered plane wave component that can contribute to an object's hologram can be determined as:

$$\cos \theta_{max} = \frac{z_2}{z_2 + \Delta L_c} \quad (6)$$

Based on this temporal coherence length consideration, for a z_2 distance of $\sim 400\text{ }\mu\text{m}$, as an example, the bandwidth of the partially coherent light source needs to be smaller than 20 nm in order to achieve a resolution of $\sim 1\text{ }\mu\text{m}$ (which is close to the pixel size).

For a narrower illumination bandwidth, and assuming that the spatial coherence does not pose a limitation, then the resolution of an on-chip holographic microscope is limited by the under-sampling that is created by the pixel pitch of the sensor chip, which can be overcome using e.g., pixel super-resolution techniques that will be discussed next.

2.2. Pixel super-resolution for on-chip holographic imaging

As discussed in the previous section, one limiting factor for resolution in an on-chip holographic microscope is pixelation and the related under-sampling of spatial frequency information at the hologram plane. To achieve resolution beyond the pixel-pitch limit, we can employ a technique called pixel super-resolution (PSR) [38–40]. In PSR, the object's hologram is shifted laterally in sub-pixel increments, and at each location on the shifting grid, a low resolution (LR) hologram is captured. This relative lateral shift of the hologram with respect to the sensor array plane can be achieved by e.g., shifting the image sensor chip [4], the sample [41], or the illumination source [40,42]. In a portable on-chip imaging device, the mechanical shifts required for PSR can be replaced by an array of LEDs that are sequentially turned on/off to cast sub-pixel shifted holograms of a static sample [42]. Using multiple LR holograms, a higher-resolution hologram can be digitally synthesized. One algorithm that can be used for this purpose is called “shift-and-add”, in which the low-resolution holograms are up-sampled, shifted, and digitally added [43].

The shift-and-add algorithm, although simple in concept and computation, is based on the assumption that the LR holograms are sub-pixel shifted on a *uniform* grid, and that pixel function is ideally a delta function, $\delta(x, y)$. This assumption puts part of the burden on hardware alignment and partially limits the choice of image sensors that can be used. When these assumptions for shift-and-add are harder to satisfy, more versatile techniques, which are based on e.g., iterative optimization, can also be used [39,40]. These iterative methods generally solve an optimization problem to minimize a cost function such as:

$$x^* = \arg \min_x \sum_i \|W_i \cdot x - y_i\|_p^q + \alpha \cdot \gamma(x) \quad (7)$$

This cost function typically contains two parts: the first part $\sum_i \|W_i \cdot x - y_i\|_p^q$ uses some norm (e.g., $p = 1$ or 2 with $q = 1$ or 2 , respectively) to minimize the distance between the optimal solution (x^*) and i different measurements, where W_i represents the digital process of shifting and down-sampling of an image and y_i is a lower resolution measurement. The second part $\gamma(x)$ is a regularization parameter to maintain/regulate some desired quality in the reconstructed image, for instance, smoothness (derivative) [39], sparsity (l_1 -norm) [44], or sparsity in its derivative (total variation) [38,45], where α serves as a coefficient that balances the strength of this regularization term. Since the transformations represented by W_i are linear, this cost function is typically convex [46], and can be optimized via convex optimization algorithms, for instance, gradient-based and conjugate-gradient based descent algorithms [39,43]. Through iterations, some of the spatial artifacts that are typically present in “shift-and-add” based solutions due to the non-uniform shift grid or finite pixel function, can be minimized. When applied to digital holographic on-chip imaging [40], the high frequency fringes of an object's hologram become quite visible after PSR (see Fig. 2(d–e)), which is used to reconstruct higher resolution images of the samples. By using PSR with a vertical only illumination angle, we were able to resolve periodic structures with a line-width as small as ~ 300 nm at 530 nm illumination wavelength, equivalent to an effective numerical aperture (NA) of ~ 0.9 (Fig. 2(f)) [8,47]. The next sub-section will discuss how this resolution can further be improved by using the diversity of illumination angles.

In addition to sampling sub-pixel shifted holograms through e.g., source, sample or sensor shifting, coherent imaging also offers other methods to achieve super-resolved pixels, for instance, by varying the illumination wavelengths with small increments (e.g., ~ 2 – 3 nm) [48], or by varying the propagation distances (i.e., z_2) [49,50]. Some recent work has also used deep-learning to achieve PSR [51–55], also covering microscopy applications [55].

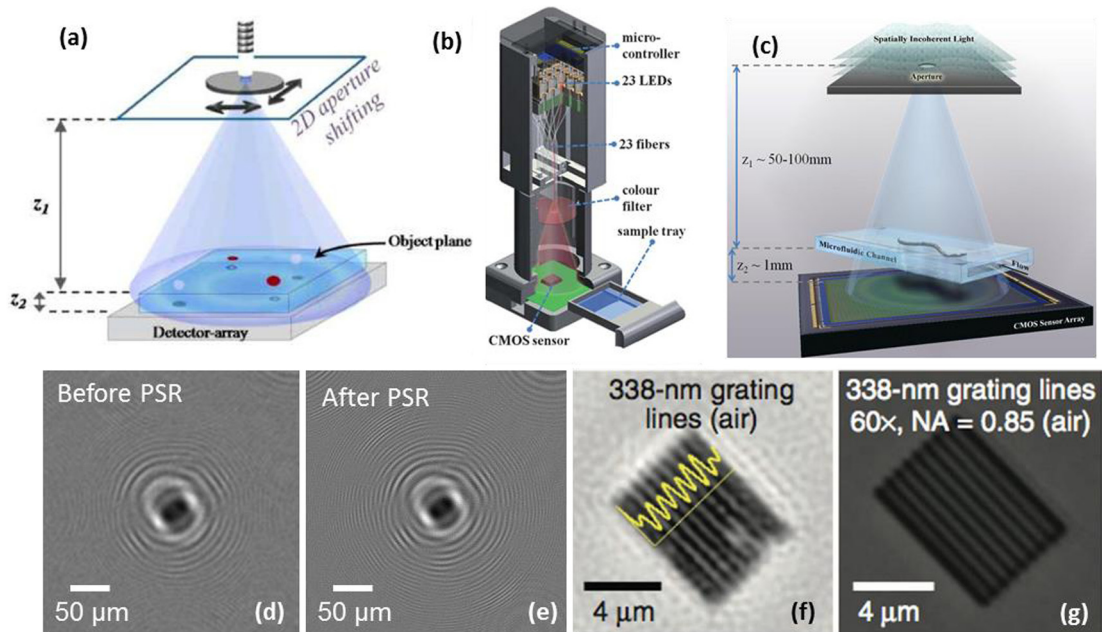


Fig. 2. Pixel super-resolution (PSR) for digital holographic on-chip imaging. Subpixels shifts in a digital hologram can be achieved through (a) source shifting, (b) an array of static light sources, e.g., fiber-coupled LEDs that are individually controllable, sensor shifting, or (c) sample shifting using e.g., a micro-fluidic flow. (d) An in-line hologram before PSR. (e) Pixel super-resolved version of the same object's hologram. (f) Reconstructed gratings with 338 nm line-width using PSR. (g) Microscope comparison of the same region of interest. Images reprinted from Refs. [8] and [40–42].

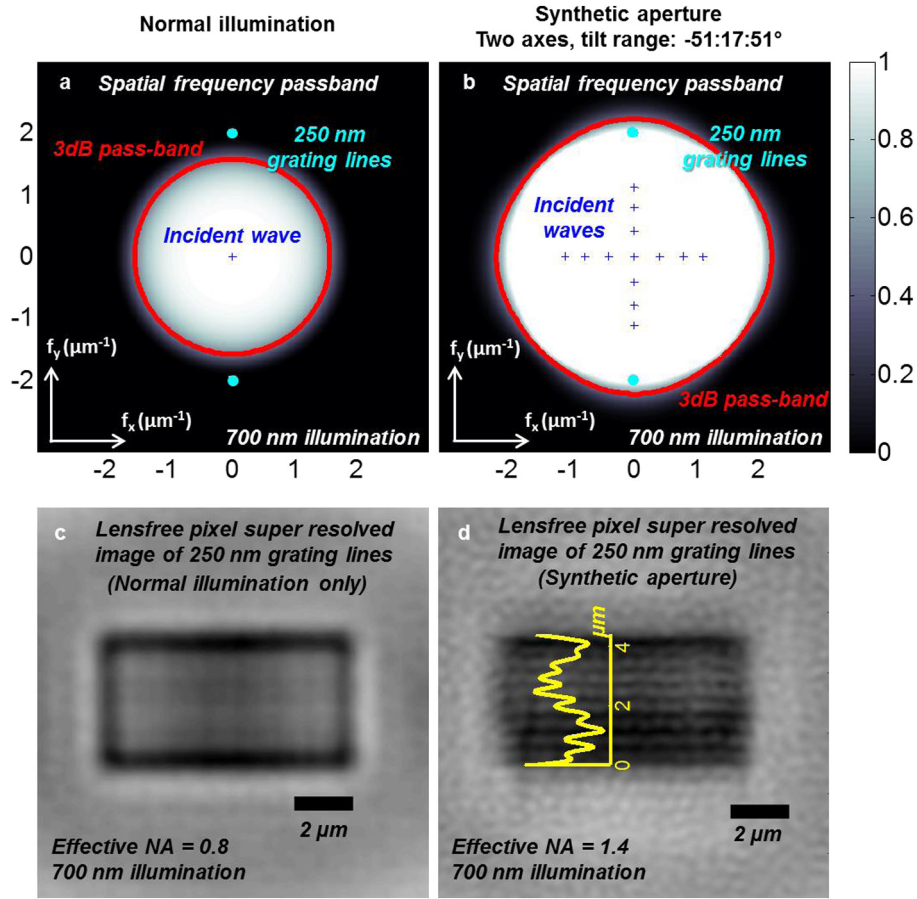


Fig. 3. Synthetic aperture based lens-less on-chip microscopy. (a,b) Spatial frequency pass-band of vertical-only (i.e., normal) illumination and after synthetic aperture method. (c,d) Lens-less holographic reconstruction of 250 nm grating lines without and with the synthetic aperture approach. Reprinted from Ref. [32].

2.3. Illumination angle diversity for enhanced resolution: synthetic aperture microscopy

The idea of synthetic aperture imaging dates back to 1950s where it was used for synthetic aperture radar [56]. Later in 1990s, it was adopted to synthetic aperture microscopy (SAM) [57,58]. In SAM, a sequence of images of the sample is captured as a function of the illumination angle with respect to the sample. Each one of these tilted illuminations provides a modulation of the frequency components of the sample that shifts the center frequencies away from the zero frequency, and at the same time, some of the high frequency components are shifted to lower frequencies. As a result, for a two dimensional (2D) object that is approximately confined to a plane, the reconstructed image can have a higher effective NA than the refractive index (n) of the medium that fills the space between the sample and sensor planes. Theoretically, an effective NA of $1 + n$ can be achieved using this synthetic aperture approach, assuming that the medium between the source and the sample planes is air. Similar ideas of shifting the high frequency components of a sample into the low-frequencies can also be achieved using structured illumination [59]. Despite computationally achieving effective NAs that are larger than n , none of these techniques can be considered to beat the diffraction limit of light as they are entirely based on propagating waves that are resulting from coherent light-matter interaction.

In a lensless on-chip microscope, SAM can be easily achieved by rotating a fiber-coupled partially coherent light source in two orthogonal directions using e.g., a rotation stage [32]. At each tilted illumination angle, source-shifting based PSR is performed to

ensure sufficient spatial sampling. This synthetic aperture approach has achieved the highest resolution reported in lensless on-chip imaging so far, which is demonstrated by resolving a grating of 250 nm line-width at an illumination wavelength of 700 nm (Fig. 3(d)), resulting in an equivalent NA of 1.4 [32].

2.4. Digital hologram reconstruction

In digital holography, the image of a sample, both amplitude and phase, can be reconstructed through a digital back-propagation step. One method of digital back-propagation is the *angular spectrum method* [10]. In this angular spectrum method, a complex wave is first transformed into spatial frequency (Fourier) domain, multiplied by a propagation kernel which is a function of the propagation distance (z_2) and is finally transformed back into the spatial domain, using e.g., Fast Fourier Transforms (FFTs). This back-propagation step converts the object's hologram into four different terms:

$$R[-z_2]\{A^* \cdot I(x, y)\} = |A|^2 \cdot [1 + \Delta t(x, y) + R[-2z_2]\{\Delta t^*(x, y)\}] + R[-z_2]\{|a(x, y)|^2\} \quad (8)$$

where the first term on the right-side is a DC-background, the second term is the reconstructed object function, the third term is the twin image artifact and the fourth term is the back-propagated self-interference term. In some imaging applications [17,18], where the objects of interest are small and relatively isolated/sparse, the twin image does not pose a significant challenge for the quality of the reconstructed image, and a simple back-propagation can then be

sufficient for these applications. In others, the image quality would be compromised by the twin image and self-interference related noise terms, thus needs to be improved using e.g., phase retrieval techniques. This is related to the fact that the recorded hologram has only amplitude information and its phase is initially missing [60].

One of the basic phase retrieval methods uses an object mask constraint [9,60], where a threshold defines a 2D mask on the object plane, and parts of the back-propagated hologram on the object plane that lie outside of the mask regions are considered noise and are iteratively removed. In addition to thresholding, this 2D object mask/support can also be defined through a microscope image of the same region, using e.g., a hybrid design that includes a traditional lens-based microscope as well as a lensless on-chip microscope [61]. This object-mask constraint works very well for imaging objects that are relatively small and isolated with a clear boundary. However, for samples that are confluent and connected, e.g., tissue slides or blood smears, it is more challenging to depict an object mask. More advanced algorithms using additional measurement constraints are needed for phase retrieval in these types of spatially dense and connected samples, which will be detailed in the next sub-sections. Furthermore, as will be briefly discussed in Section 2.7, there are also emerging deep-learning and convolutional neural network based holographic image reconstruction and phase recovery methods that achieve excellent elimination of twin image noise and self-interference related spatial artifacts even for a dense and connected sample and using a single measurement constraint [62].

2.5. Phase-retrieval using multi-height measurements

For imaging dense and connected samples, phase retrieval methods that use additional measurements at different sample-to-sensor distances (heights) can be used. These lensless holo-

graphic measurements at different heights impose physical measurement constraints that the twin image and other sources of noise terms do not satisfy. From these multiple lensless measurements at different heights, a complex-valued object function can be retrieved numerically, by digitally propagating among different measurement planes and replacing the amplitude of the calculated field at each plane by the square root of the measured intensity, while keeping the phase information unchanged. This process can be repeated for e.g., 10–30 iterations until a converged phase solution is achieved. The general framework of this type of an algorithm is called the Gerchberg-Saxton iterative error-reduction method [60,63]. In different publications, it is also referred to as the iterative projection method [64,65], or the multi-height phase retrieval algorithm [4,12,66].

In lensless on-chip imaging, the multi-height phase recovery process typically requires 6–8 heights to efficiently suppress the twin image noise and other spatial artifacts. Because the phase retrieval problem is in general not convex, the solution may stagnate at a local optimum, which is also known as the phase stagnation problem [4,67]. One way to tackle this is to have an initial phase guess that is closer to the global optimum. The transport of intensity equation (TIE) [68,69] has been demonstrated to be effective in providing an initial phase guess for the iterative multi-height phase retrieval to enable rapid convergence [4]. Using this framework, lensless on-chip imaging of pathology slides with a resolution and image quality/contrast comparable to a high-end conventional compound microscope has been demonstrated (Fig. 4) [4,70]. In another study, a field-portable and cost-effective lensless on-chip microscope based on the same multi-height phase retrieval method was also demonstrated [34,71].

A recent work, inspired by the fact that almost all natural images, including those of biological samples, are sparse in the wavelet domain, has demonstrated that e.g., CDF9/7 encoding can be used to simplify the phase retrieval process in lensless

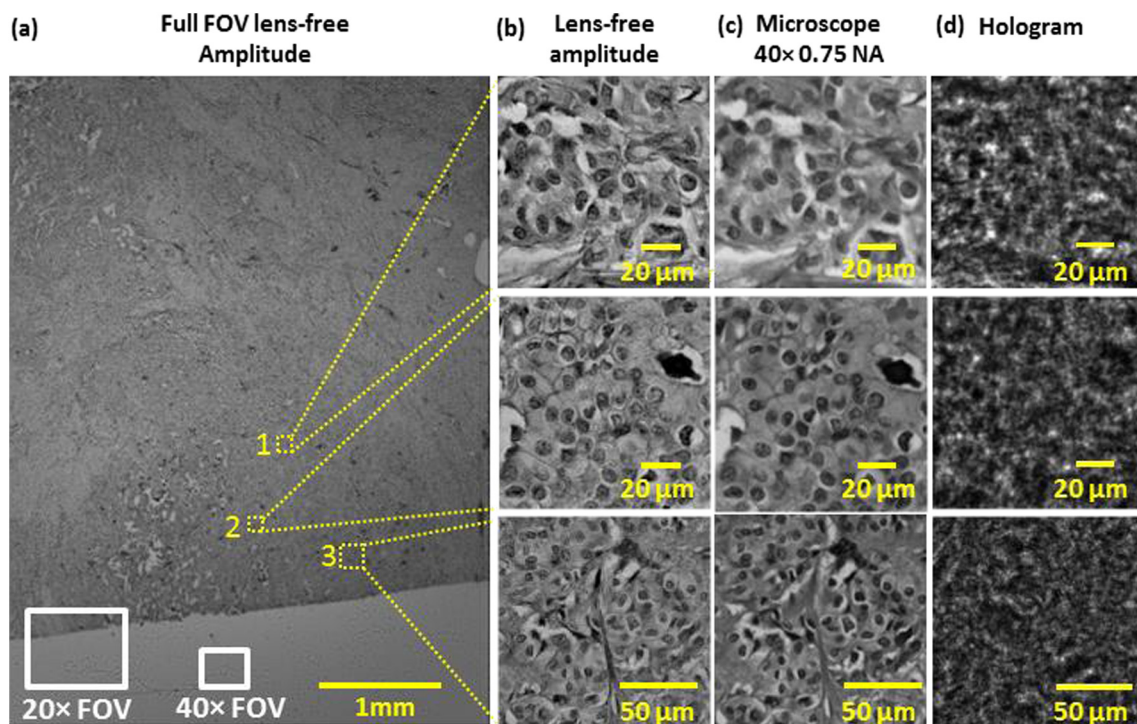


Fig. 4. Lens-free imaging of invasive ductal carcinoma of the human breast. (a) Full field-of-view (FOV) lens-free amplitude image of the specimen. For comparison, the typical digital FOV of conventional 20 \times and 40 \times microscope objectives are shown by solid rectangles. (b) Zoomed-in regions outlined by the yellow squares in (a), showing a disordered epithelium. (c) Microscope comparison image of (b) taken with a 40 \times objective lens (0.75 NA). (d) Super-resolved lens-free holograms that are used to generate the images shown in (b). Reprinted from Ref. [4]. (For interpretation of the references to colour in this figure legend, the reader is referred to the web version of this article.)

on-chip microscopy [72]. This new method, called sparsity-based multi-height phase retrieval, has demonstrated that high quality phase retrieval and image reconstruction can be achieved using only 2 heights of hologram measurements for dense and connected biological samples, instead of the 6–8 heights employed in the regular multi-height phase retrieval method, giving a significant reduction in the number of measurements required. We will discuss other applications of sparse signal recovery and compressive sensing/sampling related approaches in lensless on-chip microscopy in the next sub-section.

As another degree of freedom, multiple angles of illumination can also be used for phase retrieval, while at the same time increasing the effective NA of a reconstructed image through the synthetic aperture approach described earlier [32,49]. In addition to iterative algorithms as described above, there are also recursive phase retrieval methods that use Kalman filtering and multiple out-of-focus measurements [73,74]. Kalman filtering based recursive phase retrieval method offers good noise-reduction performance and can robustly reconstruct objects even under noise. A later work has also simplified the computational cost of this Kalman filtering based approach using a diagonal approximation of the correlation matrix [75]. However, these methods require more number of measurements (e.g., 50–100 heights) compared to iterative multi-height phase retrieval techniques (e.g., 2 heights) and their performance for high resolution imaging of dense and connected biological samples is relatively inferior in lensless on-chip imaging.

2.6. Compressive sensing/sampling and sparsity based phase retrieval

Compressive sensing or sampling framework aims to reconstruct a signal (x) using measurements (y) of much smaller dimension ($\dim(x) \gg \dim(y)$), i.e., the measurement system (matrix A) is under-determined. The basic assumption is that the signal to be reconstructed can be represented as a sparse function in some encoding domain. The compressive sensing/sampling inherently solves an optimization problem to recover a signal, x :

$$x^* = \arg \min \|Ax - y\|_p^q + \alpha \cdot \text{card}(Cx) \quad (9)$$

where α is a regularization parameter, C is the encoding matrix, $\text{card}(\cdot)$ is the cardinality function, which minimizes the number of non-zero elements in Cx . Under some assumptions [46], the above non-convex problem can be equivalent to the following convex optimization problem:

$$x^* = \arg \min \|Ax - y\|_p^q + \alpha \cdot \|Cx\|_1 \quad (10)$$

The compressive sensing/sampling framework requires that the sought signal is sparse in some encoding domain $\text{range}(C)$, and that the basis of the measurement matrix A is uncorrelated with that of the encoding matrix C . The form of the encoding matrix C depends on the prior information on the sample or its image. For instance, if the image/sample itself is sparse (e.g., a fluorescently tagged object), then $C = I$ would be sufficient, where I is the identity matrix. As another example, if the image's derivative is sparse (i.e., only a few jumps in the image), then C can simply be selected as a 2D gradient operator D , and $\text{TV}(x) = \|Dx\|_1$ is usually called the total variation or TV-norm [76]. In statistics and machine learning literature, this is also known as the least absolute shrinkage and selection operator (LASSO) method [28,77].

Using compressive sensing/sampling, digital holographic phase retrieval performance can be significantly improved [78]. Some of the early work shows that the wave propagation itself is an efficient encoding scheme in compressive sensing, which enables e.g., single-height digital holographic phase retrieval without the need for an object mask [79], and 3D sectioning of samples from

2D holographic measurements, among other achievements [80,81]. However, these schemes that use wave propagation as a sparse encoder mostly work for objects that are relatively isolated and sparse, and cannot work with dense and connected biological samples, which is an important application of lensless microscopy. As discussed in the earlier sub-section, sparse signal recovery can also be used to image dense objects using a lensless on-chip microscope by merging it with multi-height based iterative phase recovery to reduce the number of heights that is required to 2 heights. Compressive sensing has also been used in lensless multi-spectral imaging, to demultiplex images obtained with a wavelength-multiplexed illumination [82]. Although outside the scope of this manuscript, compressive sampling/sensing based approaches have also been used to significantly increase the resolution of lensless fluorescence on-chip microscopy and undo the effects of diffraction [44,83–85].

2.7. Phase retrieval using deep-learning

Deep-learning is a branch of machine learning that uses neural networks to perform automated analysis and processing of data. Recently we have been observing a renaissance in this technology and its use in various fields of science and engineering, powered by the significant improvements in e.g., parallel computing, as well as the open-source building blocks and deep-learning design frameworks shared by some research groups and leading tech companies. One very popular type of a deep network is a convolutional neural network (CNN), which might be considered to be partially inspired by the structure of the neural visual cortex, although this biological inspiration for 'modern' deep networks is also disputed by some researchers in the field. CNN typically combines convolution layers, pooling layers, and non-linear functions, each connected to others with coefficients/weights that are randomly initialized and trained using data. In general, CNNs and deep-learning currently form one of the fastest growing areas of computer science, and have been widely applied to various tasks such as image labeling [86], style-transfer [87] and even playing games against professional human players [88].

Recently it has also been demonstrated that neural networks can be used in holographic image reconstruction and phase retrieval to compute artifact-free high-resolution images of biological samples [62]. As discussed in the previous sub-sections, phase retrieval of dense and connected samples using an on-chip holographic microscope is in general a challenging task that requires measurement diversity to converge to a robust solution. In this recent work, Rivenson et al. demonstrated that a CNN, after appropriate training, can eliminate the twin image and self-interference related noise terms and achieve phase recovery and holographic reconstruction of connected biological samples using a single hologram measurement with an image reconstruction quality that is comparable to multi-height phase retrieval results using e.g., 5 measurement heights [62]. We believe that this deep-learning enabled phase retrieval method is especially promising for compact and field-portable lens-less imaging devices, eliminating the hardware complexity needed to capture multiple holograms of the object at different sample-to-sensor distances. This will further simplify the lens-less imaging hardware and reduce its image reconstruction related computational load, and would be the key for real-time imaging of various specimens even in field settings. In this sense, the general framework of machine learning, and in specific deep learning, is not only crucial for image annotation and automated detection of specific features within a microscopic image, but is also transformative for the design and implementation of mobile computational imagers, especially for telemedicine and biomedical sensing applications, among others.

2.8. Color imaging in lensless digital holographic microscopy

In many applications, including e.g., biomedical related ones, a color image is preferred, as it provides additional information and contrast of the sample. However, holography demands a quasi-monochromatic illumination for temporal coherence considerations. To get a color image of a sample, multiple holograms under different illumination wavelengths can be acquired and digitally combined to synthesize a color image of the sample. For instance, holograms using illumination wavelengths at the red (R), green (G) and blue (B) parts of the spectrum can be sequentially recorded, reconstructed separately and then digitally merged into a color image [13,32]. This requires 3-fold increase in data acquisition compared to that of a monochrome reconstruction.

One method to have less number of measurements for color imaging is called YUV averaging [34,89]. In this approach, high resolution and high quality images (through PSR and phase retrieval, i.e., without pixelation and twin image artifacts) are only acquired at a single illumination wavelength to create the Y channel (brightness) of a color image. Two additional low resolution holograms are captured, back-propagated, and merged to get the U and V channels (color) of the image. Unfortunately, since this YUV averaging method smears the color information carried out in the U and V channels, color leakage is observed at the borders of an object (e.g., a stained cell).

Another method to improve the color imaging efficiency of an on-chip holographic microscope is to *simultaneously* use three illumination wavelengths, which effectively generates a multiplexed hologram that is formed by the summation of each hologram intensity at different color channels. This multiplexed hologram, captured through a Bayer color filter array (CFA) on a color image sensor chip, can be de-multiplexed through a matrix inverse operation using the pre-calibrated spectrum of the sensor response [90–93]. However, because the pixels of different color channels on a Bayer CFA are not at the same location, conventional demosaicing methods that rely on interpolation of different channels generate color artifacts at rapidly oscillating holographic fringes. This color artifact is much more pronounced in holography because a hologram contains high frequency fringes and through digital wave propagation, these localized color artifacts can permeate to the entire object image. This fringe-related color artifact can be digitally mitigated by using PSR to generate virtual pixels that super-impose upon each other. This approach is known as demosaiced pixel super-resolution (D-PSR) method, and has been shown to generate high-fidelity color images of stained biological samples using multi-wavelength illumination with sources that are *simultaneously* on [43,93]. An alternative technique for color imaging in a holographic on-chip microscope combines a lensless microscope with a mobile-phone based microscope, through wavelet fusion of mobile-phone microscope's low-resolution color images with a pixel super-resolved lensless reconstruction at a single wavelength [94].

2.9. Lensless 3D imaging and tomography on a chip

Although a digital holographic reconstruction can retrieve both the amplitude and phase information of a sample, holography with a single perspective is subject to shadowing related artifacts and sample-induced aberrations, and is not generally considered as a 3D tomographic imaging technique since the problem of inferring 3D information from coherent scattering data is ill-posed [81,95]. In addition to holography, the same limitations also exist in e.g., optical coherence tomography (OCT), where the sample induced aberrations to the forward propagating optical wave within the sample volume is ignored, which is also referred to as the first Born approximation. This approximation implies that each volumetric

scattering element/point in a 3D sample is assumed to be illuminated with a known phase front (e.g., planar or spherical), which is hard to satisfy especially for thick and dense samples. In general, to improve the 3D sectioning capability of a coherent imaging modality, including holographic on-chip microscopy, additional measurements and degrees of freedom are needed.

One such method involves using different angles of illumination to capture a sequence of holograms. Before a tomographic image of the specimen is reconstructed through these multi-angle holograms, using a simple triangulation approach, isolated particles can be localized and their heights can be measured with ~ 300 – 400 nm axial localization accuracy [96]. This multi-angle-illumination method can also be used to monitor the motion of micro-objects in 3D. For instance, using two different illumination angles (simultaneously on) at two different wavelengths of light, together with a monochrome CMOS imager, TW Su et al. demonstrated 3D tracking of sperm locomotion across very large sample volumes of e.g., >9 – 10 μL [18,19]. Although a monochrome imager was employed in these experiments, different illumination wavelengths at different angles were used to digitally separate the vertical and oblique perspectives of the sperm locomotion from each other and calculate the 3D position of the sperm head at each frame. This holographic monitoring platform enabled researchers to discover new locomotion patterns observed in human and animal sperms [18–20].

Different angles of illumination in digital holographic on-chip imaging can also be used to generate tomographic reconstructions. Using a filtered back-projection algorithm, also used in conventional limited angle tomography, a 3D lensless image of a specimen can be reconstructed with <3 μm axial resolution and <1 μm lateral resolution [35], which was also merged with micro-fluidics to enable tomographic imaging of 3D objects during their flow [14]. A portable, 3D-printed tomographic microscope based on this concept was also demonstrated to image biological specimens [97].

2.10. Nano-particle detection and sizing using lensless on-chip microscopy

In addition to resolution, another figure-of-merit for a microscope in general is its detection limit, which is especially important for detecting nano-particles that act as very weak antennas due to their sub-wavelength dimensions. In fact, for nano-particles, the scattering intensity is inversely proportional to the fourth power of the illumination wavelength, and therefore, a smaller wavelength is often favorable to detect nano-particles. However, the on-chip imaging configuration of a lensless holographic microscope has an inherent disadvantage when it comes to detection of nano-particles: the pixels of an imager will by and large detect the directly transmitted light, and the weak scattering from an isolated nano-particle can easily be buried under pixel noise. This is intuitively the same challenge as “trying to see the moon in a sunny day”.

One clever method to detect nano-particles using an on-chip microscope is to use each nano-particle as a nucleus for self-assembled deposition of refractive materials around each particle, thus increasing its size and scattering cross-section, effectively helping its lensless detection on a chip. In one of these methods, the substrate that has the nano-particles of interest is rinsed with a Polyethylene Glycol (PEG)-based solution, and self-assembled nano-lenses are formed around each particle on the substrate after tilting it for the removal of additional material [98,99]. In another implementation of the same basic idea, the PEG solution is placed on a simple heater reservoir, which then evaporates and condenses on the substrate, forming nano-particle–nano-lens complexes that are imaged using on-chip holography [100,101]. By monitoring the formation process of these nano-lenses using time-lapse on-chip

imaging, sizing of nano-particles as small as 40 nm with a sizing accuracy of ~ 11 nm was demonstrated using illumination at ~ 510 nm [101]. In another recent work, using ultra-violet illumination at 266 nm, in combination with self-assembled nano-lenses, nano-particles as small as 24 nm have been detected [102]. Using surface chemistry and functionalization protocols, this method can also be used to detect bio-molecules and viruses, e.g., for viral load measurements in field settings [100–103]. Although outside the scope of this review article, a similar method has also been used for fluorescent imaging of particles using low-NA imagers, demonstrating 2–3-fold enhancement of the fluorescent signal that is detected using self-assembled micro-reflectors [104].

Apart from self-assembled nano-lenses, there are other computational methods that can be used to increase the contrast and SNR of a lensless image. Specifically, for digital holographic lensless microscopy, one method is to de-convolve the measured hologram with the pixel function of the image sensor chip. The pixel function can be either measured using a near field probe or using a blind-deconvolution algorithm [47]. In another paper, a Bayesian-based estimation method has been used to correct for the hardware aberrations and numerical errors, which increased the SNR by ~ 8 dB [105].

3. Air quality monitoring using digital holography on a chip

One of the major sources of air pollution is formed by particulate matter (PM), which refers to the suspended particles in air. PM in general can penetrate human respiration system and even blood and cause allergies, various diseases and even cancer. According to the World Health Organization, PM 2.5 ($2.5 \mu\text{m}$ and smaller particles in air) is a carcinogen [106]. PM also includes bio-related aerosols such as pollen, bacterial and mold spores that may cause various diseases.

Currently available devices on the market for monitoring PM can be classified into two categories: personal and institutional. The personal ones are usually based on an optical particle counter technology, where the particles in air are driven through a channel, while a laser-source shines onto these particles and a photo diode measures the scattering intensity. The size of the particles flowing through the channel is then inferred one-by-one from this scattering measurement. These devices are relatively cheaper ($\leq \$1\text{K}$) [107]. However, due to its serial read-out scheme, both its throughput (< 3 L/min) and concentration measurement range are limited. Moreover, this method is inaccurate because the scattering cross section it measures also depends on the particle shape and material (i.e., its refractive index), not just the size of the particle. The institutional devices for monitoring PM, on the other hand, have much higher throughput (~ 15 L/min) and are more accurate. These institutional platforms use e.g., beta-attenuation-monitoring (BAM) or tapered element oscillating microbalance (TEOM) based instruments [108]. For example, BAM accumulates PM of specific cut-off size on a rotating filter, and measures the attenuation induced by these captured particles using a beta-particle source and detector. The TEOM instrument, on the other hand, captures PM in a filter cartridge, and correlates the PM mass concentration to the vibrating frequency of a glass tube tip inside the cartridge. Unfortunately, these devices are usually rather bulky, heavy (~ 30 kg), expensive ($\geq \$50\text{K}$), and require specialized personnel for regular system maintenance, even daily in some cases.

None of the above-discussed PM monitoring devices gives a direct measure, i.e., a microscopic image of the captured/detected particles. Imaging-based microscopic analysis of PM can be considered as a gold-standard method. Moreover, through microscopic images, a group of aerosols and bio-aerosols can be distinguished from each other and classified through their spatial and/or spectral

characteristics. Currently, for such microscopic analyses of PM, the sample is taken in the field and the analysis is performed in a lab. For example, the aerosol sampling process in the field can use various sampling methods, including impaction, cyclone [109,110], electrostatic capturing [111], thermophoresis [112], and filtering [113]. Then the collected and fixed aerosol samples are sent to a remote laboratory, where a micro-biologist or microscopist examines the sample and prepares a report on it. As an example, a widely used method to study pollen is to collect them using a device called “Hirst Trap” [114], and after accumulation, the sample is sent to a lab, where an expert examines it under a microscope to determine the count and type of pollens detected. A similar process is also used for mold detection in e.g., buildings. Obviously, these manual lab inspection-based approaches are very slow, time-consuming and expensive, and there is an urgent need for mobile and cost-effective technologies that can rapidly and accurately measure the concentration of such bio-aerosols in the field, away from a lab. For this ambitious goal lensless holographic on-chip imaging offers numerous advantages as will be discussed next.

3.1. c-Air: a hand-held, accurate, cost-effective and high-throughput PM monitor based on machine learning

Recently, a new platform termed c-Air was introduced for the measurement of PM that combines a lensless on-chip microscope with an impaction-based air sampler, offering accurate and high-throughput air quality monitoring in a field-portable and cost-effective device (Fig. 5(b)) [23]. The letter “c” in c-Air stands for “computational imaging”, while at the same time c-Air is homophonic to “see-Air”, referring to the fact that it is a computational imaging-based air quality monitor. c-Air has a throughput of ~ 13 L/min and weighs ~ 590 g and is wirelessly controlled by a custom-designed smartphone application. A current prototype of c-Air costs $< \$150$ in parts, even using extremely low volume of manufacturing. c-Air is based on an “impactor-on-chip” geometry (Fig. 5(a)), where the air is sucked in through the impactor nozzle by a small pump and the particles inside air are captured on a sticky transparent coverslip directly facing the air stream. These captured particles, illuminated by fiber-coupled LEDs, then cast in-line holograms on the image sensor chip, which are sent wirelessly to a remote server for image reconstruction, processing and particle size/density analysis.

On the server side, a differential analysis of the captured holograms is applied, where the differences between two successive holograms (one before the air sample is introduced and one right after it) represent the newly captured aerosols on the cartridge. Then an iterative algorithm detects the particles, starting from the larger sizes toward the smaller ones, with the help of a machine learning based approach (i.e., using support vector machine, SVM) that is used to exclude potential reconstruction artifacts and eliminate false positives. The smallest particle that can be reliably captured by the impactor in c-Air is around $1 \mu\text{m}$, although smaller particles can also be detected with some changes to our device design. Following this particle detection step, another machine learning algorithm based on a statistically learned linear mapping using a second-order polynomial model is utilized to size the particles, achieving a sizing accuracy of $\sim 93\%$ (Fig. 5(c)). This is then used to generate a size/density histogram of the particles and other statistics of the PM. The measurement results are also spatially-stamped using the GPS coordinates of the smartphone that controls the device.

This portable c-Air device shows high accuracy in monitoring PM, which is confirmed through a side-by-side comparison against an Environmental Protection Agency (EPA)-approved BAM PM2.5 device (Fig. 5(d)). The c-Air device is subsequently taken to various

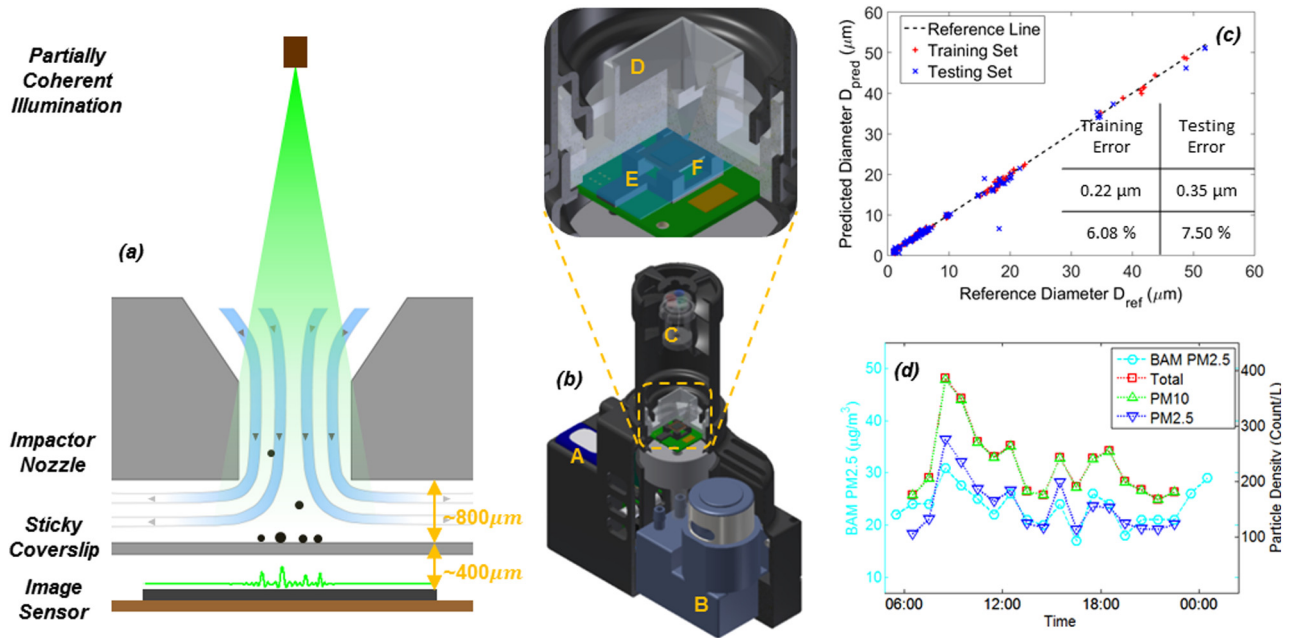


Fig. 5. c-Air device and air quality measurement results. (a) Schematics of c-Air. (b) CAD drawing of the device, including (A) a rechargeable battery, (B) a vacuum pump (with a throughput of 13 L/min), (C) LED illumination, (D) an impaction-based air sampler with (E) a sticky coverslip on top of (F) a CMOS image sensor chip. The entire device weighs ~ 590 g and is wirelessly controlled by a custom-designed smartphone application. (c) Machine learning achieves a particle sizing accuracy of $\sim 93\%$. (d) The c-Air PM measurement results (right y-axis) against the results of an EPA-approved BAM PM2.5 device (left y-axis), showing a close agreement with each other. The figure is rearranged from Ref. [23].

locations to measure the air quality in indoor and outdoor environments. One of our measurements showed a significantly increased PM in Westwood, Los Angeles area during a wild forest fire that was >40 km away from the measurement site (Sand Fire [115]). c-Air prototypes were also used to perform a 24-h spatio-temporal mapping of the PM around the Los Angeles International Airport (LAX), which showed that the PM concentrations are strongly modulated by the total number of flights at LAX. This modulation is even prominent for >7 km away from LAX along the direction of landing flights [23]. The same trend was also independently confirmed by another spatio-temporal air quality mapping experiment around LAX using a lower throughput, bulky and significantly more expensive commercial air quality monitor [116].

By further employing machine learning based particle identification and classification algorithms, this lensless imaging-based air quality measurement device, c-Air, can be used to automatically monitor bio-aerosols, such as pollen, bacteria or mold spores, eliminating the need to send the specimen to microbiology labs, and creating a valuable opportunity to rapidly and cost-effectively conduct these bio-aerosol measurements in field settings.

4. Outlook

There are several areas where lensless on-chip microscopy can be further improved. In terms of the basic imaging framework, we anticipate that the hardware of the system will continuously improve benefiting from consumer grade image sensor technologies (especially built for mobile devices, including smartphones) and computational power of modern computers. Smarter measurement strategies and reconstruction methods will continue to improve the efficiency of performing PSR, phase-retrieval [49,72], and color imaging [93] methods, potentially enabling real-time reconstructions over large sample volumes. Algorithm efficiency and image reconstruction times are posed to significantly improve using novel signal processing methods including semi-definite pro-

gramming (SDP) [117,118], proximal projection optimization [119], and deep-learning [62]. Migrating the entire computation that is needed for a lensless on-chip microscope to parallel computing using GPUs can also further decrease the reconstruction times by e.g., >10 – 100 -fold [13].

In terms of field-portable lensless microscopy, further improvements in the capabilities of the system and its cost-effectiveness will help its wide scale deployment and use. For the specific case of air quality monitoring, a more compact and even lighter device based on the c-Air platform can be widely deployed along highways and residential areas, among others, and carried effortlessly by bikers, hikers and even toy drones. Working together, these devices on the ground and in air will constitute a dense and smart air quality monitoring network, helping us better understand various sources of contamination as a function of both space and time. Similar smart networks for monitoring water pollution can also be constructed by integrating lensless on-chip microscopy and cytometry tools with cost-effective toy sub-marines.

Acknowledgements

The Ozcan Research Group at UCLA acknowledges the support of the Presidential Early Career Award for Scientists and Engineers (PECASE), the Army Research Office (ARO; W911NF-13-1-0419 and W911NF-13-1-0197), the ARO Life Sciences Division, the National Science Foundation (NSF) CBET Division Biophotonics Program, the NSF Emerging Frontiers in Research and Innovation (EFRI) Award, the NSF EAGER Award, NSF INSPIRE Award, NSF Partnerships for Innovation: Building Innovation Capacity (PFI:BIC) Program, Office of Naval Research (ONR), the National Institutes of Health (NIH), the Howard Hughes Medical Institute (HHMI), Vodafone Americas Foundation, the Mary Kay Foundation, Steven & Alexandra Cohen Foundation, and KAUST. This work is based upon research performed in a laboratory renovated by the National Science Foundation under Grant No. 0963183, which is an award

funded under the American Recovery and Reinvestment Act of 2009 (ARRA).

References

- [1] D. Bardell, The Biologists' Forum: the invention of the microscope, BIOS 75 (2004) 78–84, [http://dx.doi.org/10.1893/0005-3155\(2004\)75:78:TIOTM>2.0.CO;2](http://dx.doi.org/10.1893/0005-3155(2004)75:78:TIOTM>2.0.CO;2).
- [2] E. McLeod, A. Ozcan, Unconventional methods of imaging: computational microscopy and compact implementations, Rep. Prog. Phys. 79 (2016) 076001, <http://dx.doi.org/10.1088/0034-4885/79/7/076001>.
- [3] A. Ozcan, Mobile phones democratize and cultivate next-generation imaging, diagnostics and measurement tools, Lab Chip 14 (2014) 3187–3194.
- [4] A. Greenbaum, Y. Zhang, A. Feizi, P.-L. Chung, W. Luo, S.R. Kandukuri, A. Ozcan, Wide-field computational imaging of pathology slides using lens-free on-chip microscopy 267ra175–267ra175, Sci. Transl. Med. 6 (2014), <http://dx.doi.org/10.1126/scitranslmed.3009850>.
- [5] G. Brooker, N. Siegel, J. Rosen, N. Hashimoto, M. Kurihara, A. Tanabe, In-line FINCH super resolution digital holographic fluorescence microscopy using a high efficiency transmission liquid crystal GRIN lens, Opt. Lett. 38 (2013) 5264–5267.
- [6] V. Bianco, M. Paturzo, V. Marchesano, I. Gallotta, E. Di Schiavi, P. Ferraro, Optofluidic holographic microscopy with custom field of view (FoV) using a linear array detector, Lab Chip 15 (2015) 2117–2124.
- [7] G.P. Laporte, N. Stasio, C.J. Sheppard, D. Psaltis, Resolution enhancement in nonlinear scanning microscopy through post-detection digital computation, Optica 1 (2014) 455–460.
- [8] A. Greenbaum, W. Luo, T.-W. Su, Z. Göröcs, L. Xue, S.O. Isikman, A.F. Coskun, O. Mudanyali, A. Ozcan, Imaging without lenses: achievements and remaining challenges of wide-field on-chip microscopy, Nat. Methods 9 (2012) 889–895.
- [9] O. Mudanyali, D. Tseng, C. Oh, S.O. Isikman, I. Sencan, W. Bishara, C. Oztoprak, S. Seo, B. Khademhosseini, A. Ozcan, Compact, light-weight and cost-effective microscope based on lensless incoherent holography for telemedicine applications, Lab Chip 10 (2010) 1417–1428, <http://dx.doi.org/10.1039/C000453G>.
- [10] J.W. Goodman, Introduction to Fourier Optics (accessed December 18, 2015), 3rd ed., Roberts and Company Publishers, 2005 (accessed December 18, 2015).
- [11] Y. Zhang, S.Y.C. Lee, Y. Zhang, D. Furst, J. Fitzgerald, A. Ozcan, Wide-field imaging of birefringent synovial fluid crystals using lens-free polarized microscopy for gout diagnosis, Sci. Rep. 6 (2016), <http://dx.doi.org/10.1038/srep28793>.
- [12] Y. Zhang, A. Greenbaum, W. Luo, A. Ozcan, Wide-field pathology imaging using on-chip microscopy, Virchows Arch. 467 (2015) 3–7, <http://dx.doi.org/10.1007/s00428-015-1782-z>.
- [13] S.O. Isikman, I. Sencan, O. Mudanyali, W. Bishara, C. Oztoprak, A. Ozcan, Color and monochrome lensless on-chip imaging of Caenorhabditis elegans over a wide field-of-view, Lab Chip 10 (2010) 1109–1112, <http://dx.doi.org/10.1039/C001200A>.
- [14] S.O. Isikman, W. Bishara, H. Zhu, A. Ozcan, Optofluidic tomography on a chip, Appl. Phys. Lett. 98 (2011) 161109.
- [15] O. Mudanyali, C. Oztoprak, D. Tseng, A. Erlinger, A. Ozcan, Detection of waterborne parasites using field-portable and cost-effective lensfree microscopy, Lab Chip 10 (2010) 2419–2423.
- [16] A. Feizi, Y. Zhang, A. Greenbaum, A. Guziak, M. Luong, R.Y.L. Chan, B. Berg, H. Ozkan, W. Luo, M. Wu, Y. Wu, A. Ozcan, Rapid, portable and cost-effective yeast cell viability and concentration analysis using lensfree on-chip microscopy and machine learning, Lab Chip (2016), <http://dx.doi.org/10.1039/C6LC00976j>.
- [17] T.-W. Su, A. Erlinger, D. Tseng, A. Ozcan, Compact and light-weight automated semen analysis platform using lensfree on-chip microscopy, Anal. Chem. 82 (2010) 8307–8312.
- [18] T.-W. Su, L. Xue, A. Ozcan, High-throughput lensfree 3D tracking of human sperms reveals rare statistics of helical trajectories, Proc. Natl. Acad. Sci. 109 (2012) 16018–16022, <http://dx.doi.org/10.1073/pnas.1212506109>.
- [19] T.-W. Su, I. Choi, J. Feng, K. Huang, E. McLeod, A. Ozcan, Sperm trajectories form chiral ribbons, Sci. Rep. 3 (2013), <http://dx.doi.org/10.1038/srep01664>.
- [20] T.-W. Su, I. Choi, J. Feng, K. Huang, A. Ozcan, High-throughput analysis of horse sperms' 3D swimming patterns using computational on-chip imaging, Anim. Reprod. Sci. 169 (2016) 45–55, <http://dx.doi.org/10.1016/j.anireprosci.2015.12.012>.
- [21] W. Luo, F. Shabbir, C. Gong, C. Gulec, J. Pigeon, J. Shaw, A. Greenbaum, S. Tochitsky, C. Joshi, A. Ozcan, High throughput on-chip analysis of high-energy charged particle tracks using lensfree imaging, Appl. Phys. Lett. 106 (2015) 151107.
- [22] K.-W. Huang, T.-W. Su, A. Ozcan, P.-Y. Chiou, Optoelectronic tweezers integrated with lensfree holographic microscopy for wide-field interactive cell and particle manipulation on a chip, Lab Chip 13 (2013) 2278–2284.
- [23] W. Yichen, S. Ashutosh, L. Yicheng, W. Jeffrey, F. Steve, C. Xuan, C. Christine, J. Kevin, J. Saba, Y. Zhe, B. Zachary, G. Zoltán, F. Alborz, O. Aydogan, Air quality monitoring using mobile microscopy and machine learning, Light Sci. Appl. (2017), <http://dx.doi.org/10.1038/lsa.2017.46>.
- [24] S. Seo, S.O. Isikman, I. Sencan, O. Mudanyali, T.-W. Su, W. Bishara, A. Erlinger, A. Ozcan, High-throughput lens-free blood analysis on a chip, Anal. Chem. 82 (2010) 4621–4627, <http://dx.doi.org/10.1021/ac1007915>.
- [25] A.F. Coskun, A.E. Cetin, B.C. Galarreta, D.A. Alvarez, H. Altug, A. Ozcan, Lensfree optofluidic plasmonic sensor for real-time and label-free monitoring of molecular binding events over a wide field-of-view, Sci. Rep. 4 (2014) (accessed September 16, 2015) http://www.nature.com/srep/2014/141027/srep06789/full/srep06789.html?WT.ec_id=SREP-639-20141028.
- [26] A.E. Cetin, A.F. Coskun, B.C. Galarreta, M. Huang, D. Herman, A. Ozcan, H. Altug, Handheld high-throughput plasmonic biosensor using computational on-chip imaging, Light Sci. Appl. 3 (2014) e122.
- [27] B. Khademhosseini, G. Biener, I. Sencan, T.-W. Su, A.F. Coskun, A. Ozcan, Lensfree sensing on a microfluidic chip using plasmonic nanoapertures, Appl. Phys. Lett. 97 (2010) 221107.
- [28] Z.S. Ballard, D. Shir, A. Bhardwaj, S. Bazargan, S. Sathianathan, A. Ozcan, Computational sensing using low-cost and mobile plasmonic readers designed by machine learning, ACS Nano 11 (2017) 2266–2274, <http://dx.doi.org/10.1021/acsnano.7b00105>.
- [29] Q. Wei, E. McLeod, H. Qi, Z. Wan, R. Sun, A. Ozcan, On-chip cytometry using plasmonic nanoparticle enhanced lensfree holography, Sci. Rep. 3 (2013), <http://dx.doi.org/10.1038/srep01699>.
- [30] A. Ozcan, E. McLeod, Lensless imaging and sensing, Annu. Rev. Biomed. Eng. 18 (2016) 77–102, <http://dx.doi.org/10.1146/annurev-bioeng-092515-010849>.
- [31] S. Seo, T.-W. Su, D.K. Tseng, A. Erlinger, A. Ozcan, Lensfree holographic imaging for on-chip cytometry and diagnostics, Lab Chip 9 (2009) 777–787.
- [32] W. Luo, A. Greenbaum, Y. Zhang, A. Ozcan, Synthetic aperture-based on-chip microscopy, Light Sci. Appl. 4 (2015) e261, <http://dx.doi.org/10.1038/lsa.2015.34>.
- [33] D. Tseng, O. Mudanyali, C. Oztoprak, S.O. Isikman, I. Sencan, O. Yaglidere, A. Ozcan, Lensfree microscopy on a cellphone, Lab Chip 10 (2010) 1787–1792.
- [34] A. Greenbaum, N. Akbari, A. Feizi, W. Luo, A. Ozcan, Field-portable pixel super-resolution colour microscope, PLoS One 8 (2013) e76475.
- [35] S.O. Isikman, W. Bishara, S. Mavandadi, W.Y. Frank, S. Feng, R. Lau, A. Ozcan, Lens-free optical tomographic microscope with a large imaging volume on a chip, Proc. Natl. Acad. Sci. 108 (2011) 7296–7301.
- [36] M. Born, E. Wolf, Principles of optics: electromagnetic theory of propagation, interference and diffraction of light, CUP Archive, 2000. <https://books.google.com/books?hl=en&lr=&id=oV80AAAAIAAJ&oi=fnd&pg=PR25&dq=principle+of+optics+born&ots=y0TWxSU0IN&sig=JgfvKHuGvShdGnqsVADgtjdJLcg> (accessed June 9, 2016).
- [37] J.W. Goodman, Statistical Optics, John Wiley & Sons, 2015.
- [38] S. Farsiu, M.D. Robinson, M. Elad, P. Milanfar, Fast and robust multiframe super resolution, IEEE Trans. Image Process. 13 (2004) 1327–1344, <http://dx.doi.org/10.1109/TIP.2004.834669>.
- [39] R.C. Hardie, K.J. Barnard, J.G. Bognar, E.E. Armstrong, E.A. Watson, High-resolution image reconstruction from a sequence of rotated and translated frames and its application to an infrared imaging system, Opt. Eng. 37 (1998) 247–260, <http://dx.doi.org/10.1117/1.601623>.
- [40] W. Bishara, T.-W. Su, A.F. Coskun, A. Ozcan, Lensfree on-chip microscopy over a wide field-of-view using pixel super-resolution, Opt. Express. 18 (2010) 11181–11191, <http://dx.doi.org/10.1364/OE.18.011181>.
- [41] W. Bishara, H. Zhu, A. Ozcan, Holographic opto-fluidic microscopy, Opt. Express. 18 (2010) 27499–27510, <http://dx.doi.org/10.1364/OE.18.027499>.
- [42] W. Bishara, U. Sikora, O. Mudanyali, T.-W. Su, O. Yaglidere, S. Luckhart, A. Ozcan, Holographic pixel super-resolution in portable lensless on-chip microscopy using a fiber-optic array, Lab Chip 11 (2011) 1276–1279, <http://dx.doi.org/10.1039/C0LC00684j>.
- [43] S. Farsiu, M. Elad, P. Milanfar, Multiframe demosaicing and super-resolution of color images, IEEE Trans. Image Process. 15 (2006) 141–159, <http://dx.doi.org/10.1109/TIP.2005.860336>.
- [44] A.F. Coskun, I. Sencan, T.-W. Su, A. Ozcan, Lensless wide-field fluorescent imaging on a chip using compressive decoding of sparse objects, Opt. Express 18 (2010) 10510–10523.
- [45] A. Chambolle, An algorithm for total variation minimization and applications, J. Math. Imaging Vis. 20 (2004) 89–97, <http://dx.doi.org/10.1023/B:JMIV.0000011325.36760.1e>.
- [46] S. Boyd, L. Vandenberghe, Convex Optimization, Cambridge University Press, 2004. https://books.google.com/books?hl=en&lr=&id=IUZdAAAAQBAJ&oi=fnd&pg=PR11&dq=convex+optimization&ots=HMKDfh1DDo&sig=Msc5_Jll19LkFNUsefxmqIOFY_E (accessed June 9, 2016).
- [47] A. Greenbaum, W. Luo, B. Khademhosseini, T.-W. Su, A.F. Coskun, A. Ozcan, Increased space-bandwidth product in pixel super-resolved lensfree on-chip microscopy, Sci. Rep. 3 (2013), <http://dx.doi.org/10.1038/srep01717>.
- [48] W. Luo, Y. Zhang, A. Feizi, Z. Gorocs, A. Ozcan, Pixel super-resolution using wavelength scanning, Light Sci. Appl. 5 (2016) e16058, <http://dx.doi.org/10.1038/lsa.2016.58>.
- [49] W. Luo, Y. Zhang, Z. Göröcs, A. Feizi, A. Ozcan, Propagation phasor approach for holographic image reconstruction, Sci. Rep. 6 (2016) 22738, <http://dx.doi.org/10.1038/srep22738>.
- [50] H. Wang, Z. Göröcs, W. Luo, Y. Zhang, Y. Rivenson, L.A. Bentolila, A. Ozcan, Computational out-of-focus imaging increases the space-bandwidth product in lens-based coherent microscopy, Optica 3 (2016) 1422–1429, <http://dx.doi.org/10.1364/OPTICA.3.001422>.
- [51] J. Kim, J.K. Lee, K.M. Lee, Accurate Image Super-Resolution Using Very Deep Convolutional Networks, ArXiv151104587 Cs. (2015). <http://arxiv.org/abs/1511.04587>.

- [52] J. Kim, J.K. Lee, K.M. Lee, Deeply-Recursive Convolutional Network for Image Super-Resolution, *ArXiv151104491* Cs. (2015). <http://arxiv.org/abs/1511.04491>.
- [53] C. Dong, C.C. Loy, K. He, X. Tang, Image super-resolution using deep convolutional networks, *IEEE Trans. Pattern Anal. Mach. Intell.* 38 (2016) 295–307, <http://dx.doi.org/10.1109/TPAMI.2015.2439281>.
- [54] W. Shi, J. Caballero, F. Huszar, J. Totz, A.P. Aitken, R. Bishop, D. Rueckert, Z. Wang, Real-Time Single Image and Video Super-Resolution Using an Efficient Sub-Pixel Convolutional Neural Network, *ArXiv160905158* Cs Stat. (2016). <http://arxiv.org/abs/1609.05158>.
- [55] Y. Rivenson, Z. Gorocs, H. Gunaydin, Y. Zhang, H. Wang, A. Ozcan, Deep learning microscopy, *ArXiv170504709* Phys. (2017). <http://arxiv.org/abs/1705.04709>.
- [56] J.C. Curlander, R.N. McDonough, *Synthetic Aperture Radar*, John Wiley & Sons, New York, NY, USA, 1991. <http://web.stanford.edu/class/ee355/handouts/handout1.pdf>.
- [57] T.M. Turpin, L.H. Gesell, J. Lapides, C.H. Price, Theory of the synthetic aperture microscope, in: 1995: pp. 230–240. doi: 10.1117/12.217378.
- [58] T.S. Ralston, D.L. Marks, P. Scott Carney, S.A. Boppart, Interferometric synthetic aperture microscopy, *Nat. Phys.* 3 (2007) 129–134, <http://dx.doi.org/10.1038/nphys514>.
- [59] M.G.L. Gustafsson, Surpassing the lateral resolution limit by a factor of two using structured illumination microscopy, *J. Microsc.* 198 (2000) 82–87, <http://dx.doi.org/10.1046/j.1365-2818.2000.00710.x>.
- [60] J. Fienup, Phase retrieval algorithms – a comparison, *Appl. Opt.* 21 (1982) 2758–2769.
- [61] G. Biener, A. Greenbaum, S.O. Isikman, K. Lee, D. Tseng, A. Ozcan, Combined reflection and transmission microscope for telemedicine applications in field settings, *Lab Chip* 11 (2011) 2738–2743.
- [62] Y. Rivenson, Y. Zhang, H. Gunaydin, D. Teng, A. Ozcan, Phase recovery and holographic image reconstruction using deep learning in neural networks, *ArXiv170504286* Phys. (2017). <http://arxiv.org/abs/1705.04286> (accessed May 14, 2017).
- [63] R.W. Gerchber, W.O. Saxton, Practical algorithm for determination of phase from image and diffraction plane pictures, *Optik* 35 (1972) 237.
- [64] V. Elser, Phase retrieval by iterated projections, *J. Opt. Soc. Am. A* 20 (2003) 40, <http://dx.doi.org/10.1364/JOSAA.20.000040>.
- [65] L.J. Allen, M.P. Oxley, Phase retrieval from series of images obtained by defocus variation, *Opt. Commun.* 199 (2001) 65–75, [http://dx.doi.org/10.1016/S0030-4018\(01\)01556-5](http://dx.doi.org/10.1016/S0030-4018(01)01556-5).
- [66] A. Greenbaum, A. Ozcan, Maskless imaging of dense samples using pixel super-resolution based multi-height lensfree on-chip microscopy, *Opt. Express* 20 (2012) 3129–3143.
- [67] J. Fienup, C. Wackerman, Phase-retrieval stagnation problems and solutions, *J. Opt. Soc. Am. – Opt. Image Sci. Vis.* 3 (1986) 1897–1907, <http://dx.doi.org/10.1364/JOSAA.3.001897>.
- [68] T.E. Gureyev, K.A. Nugent, Phase retrieval with the transport-of-intensity equation. II. Orthogonal series solution for nonuniform illumination, *JOSA A* 13 (1996) 1670–1682, <http://dx.doi.org/10.1364/JOSAA.13.001670>.
- [69] L. Waller, L. Tian, G. Barbastathis, Transport of intensity phase-amplitude imaging with higher order intensity derivatives, *Opt. Express* 18 (2010) 12552–12561, <http://dx.doi.org/10.1364/OE.18.012552>.
- [70] J. Weidling, S.O. Isikman, A. Greenbaum, A. Ozcan, E. Botvinick, Lens-free computational imaging of capillary morphogenesis within three-dimensional substrates, *J. Biomed. Opt.* 17 (2012) 126018 126018.
- [71] A. Greenbaum, U. Sikora, A. Ozcan, Field-portable wide-field microscopy of dense samples using multi-height pixel super-resolution based lensfree imaging, *Lab Chip* 12 (2012) 1242–1245.
- [72] Y. Rivenson, Y. Wu, H. Wang, Y. Zhang, A. Feizi, A. Ozcan, Sparsity-based multi-height phase recovery in holographic microscopy srep37862, *Sci. Rep.* 6 (2016), <http://dx.doi.org/10.1038/srep37862>.
- [73] L. Waller, M. Tsang, S. Ponda, S.Y. Yang, G. Barbastathis, Phase and amplitude imaging from noisy images by Kalman filtering, *Opt. Express* 19 (2011) 2805–2814.
- [74] Z. Jingshan, L. Tian, J. Dauwels, L. Waller, Partially coherent phase imaging with simultaneous source recovery, *Biomed. Opt. Express* 6 (2015) 257–265.
- [75] Z. Jingshan, J. Dauwels, M.A. Vázquez, L. Waller, Sparse ACEKF for phase reconstruction, *Opt. Express* 21 (2013) 18125–18137.
- [76] L.I. Rudin, S. Osher, E. Fatemi, Nonlinear total variation based noise removal algorithms, *Phys. Nonlinear Phenom.* 60 (1992) 259–268, [http://dx.doi.org/10.1016/0167-2789\(92\)90242-F](http://dx.doi.org/10.1016/0167-2789(92)90242-F).
- [77] R. Tibshirani, Regression shrinkage and selection via the Lasso, *J. R. Stat. Soc. Ser. B-Methodol.* 58 (1996) 267–288.
- [78] Y. Rivenson, A. Stern, B. Javidi, Overview of compressive sensing techniques applied in holography [Invited], *Appl. Opt.* 52 (2013) A423–A432.
- [79] T. Lатычевская, H.-W. Fink, Solution to the twin image problem in holography, *Phys. Rev. Lett.* 98 (2007) 233901, <http://dx.doi.org/10.1103/PhysRevLett.98.233901>.
- [80] Y. Rivenson, A. Stern, J. Rosen, Compressive multiple view projection incoherent holography, *Opt. Express* 19 (2011) 6109–6118, <http://dx.doi.org/10.1364/OE.19.006109>.
- [81] D.J. Brady, K. Choi, D.L. Marks, R. Horisaki, S. Lim, Compressive holography, *Opt. Express* 17 (2009) 13040–13049.
- [82] I. Sencan, A.F. Coskun, U. Sikora, A. Ozcan, Spectral demultiplexing in holographic and fluorescent on-chip microscopy, *Sci. Rep.* 4 (2014), <http://dx.doi.org/10.1038/srep03760>.
- [83] A.F. Coskun, I. Sencan, T.-W. Su, A. Ozcan, Wide-field lensless fluorescent microscopy using a tapered fiber-optic faceplate on a chip, *Analyst* 136 (2011) 3512–3518.
- [84] A.F. Coskun, I. Sencan, T.-W. Su, A. Ozcan, Lensfree fluorescent on-chip imaging of transgenic *Caenorhabditis elegans* over an ultra-wide field-of-view, *PLoS One* 6 (2011). e15955 e15955.
- [85] H. Zhu, S. Mavandadi, A.F. Coskun, O. Yaglidere, A. Ozcan, Optofluidic fluorescent imaging cytometry on a cell phone, *Anal. Chem.* 83 (2011) 6641–6647.
- [86] V.N. Murthy, S. Maji, R. Manmatha, Automatic image annotation using deep learning representations, in: *Proc. 5th ACM Int. Conf. Multimed. Retr.*, ACM, New York, NY, USA, 2015, pp. 603–606. doi: 10.1145/2671188.2749391.
- [87] L.A. Gatys, A.S. Ecker, M. Bethge, Image Style Transfer Using Convolutional Neural Networks, in: 2016: pp. 2414–2423. http://www.cv-foundation.org/openaccess/content_cvpr_2016/html/Gatys_Image_Style_Transfer_CVPR_2016_paper.html (accessed June 15, 2017).
- [88] D. Silver, A. Huang, C.J. Maddison, A. Guez, L. Sifre, G. van den Driessche, J. Schrittwieser, I. Antonoglou, V. Panneershelvam, M. Lanctot, S. Dieleman, D. Grewe, J. Nham, N. Kalchbrenner, I. Sutskever, T. Lillicrap, M. Leach, K. Kavukcuoglu, T. Graepel, D. Hassabis, Mastering the game of Go with deep neural networks and tree search, *Nature* 529 (2016) 484–489, <http://dx.doi.org/10.1038/nature16961>.
- [89] A. Greenbaum, A. Feizi, N. Akbari, A. Ozcan, Wide-field computational color imaging using pixel super-resolved on-chip microscopy, *Opt. Express* 21 (2013) 12469–12483.
- [90] Z. Göröcs, M. Kiss, V. Tóth, L. Orzó, S. Tokés, Multicolor digital holographic microscope (DHM) for biological purposes, in: D.L. Farkas, D.V. Nicolau, R.C. Leif (Eds.), *BIOs, International Society for Optics and Photonics*, 2010, pp. 75681P–75681P–10. doi: 10.1117/12.841962.
- [91] Z. Göröcs, L. Orzó, M. Kiss, V. Tóth, S. Tokés, In-line color digital holographic microscope for water quality measurements, in: M. Kinnunen, R. Myllylä (Eds.), *Laser Appl. Life Sci.* 2010, International Society for Optics and Photonics, 2010, pp. 737614–737614–10. doi: 10.1117/12.871098.
- [92] M.Z. Kiss, B.J. Nagy, P. Lakatos, Z. Göröcs, S. Tokés, B. Wittner, L. Orzó, Special multicolor illumination and numerical tilt correction in volumetric digital holographic microscopy, *Opt. Express* 22 (2014) 7559–7573, <http://dx.doi.org/10.1364/OE.22.007559>.
- [93] Y. Wu, Y. Zhang, W. Luo, A. Ozcan, Demosaiced pixel super-resolution for multiplexed holographic color imaging, *Sci. Rep.* 6 (2016), <http://dx.doi.org/10.1038/srep28601>.
- [94] Y. Zhang, Y. Wu, Y. Zhang, A. Ozcan, Color calibration and fusion of lens-free and mobile-phone microscopy images for high-resolution and accurate color reproduction, *Sci. Rep.* 6 (2016) 27811, <http://dx.doi.org/10.1038/srep27811>.
- [95] A.J. Devaney, Nonuniqueness in the inverse scattering problem, *J. Math. Phys.* 19 (1978) 1526–1531, <http://dx.doi.org/10.1063/1.523860>.
- [96] T.-W. Su, S.O. Isikman, W. Bishara, D. Tseng, A. Erlinger, A. Ozcan, Multi-angle lensless digital holography for depth resolved imaging on a chip, *Opt. Express* 18 (2010) 9690–9711.
- [97] S.O. Isikman, W. Bishara, U. Sikora, O. Yaglidere, J. Yeah, A. Ozcan, Field-portable lensfree tomographic microscope, *Lab Chip* 11 (2011) 2222–2230.
- [98] O. Mudanyali, W. Bishara, A. Ozcan, Lensfree super-resolution holographic microscopy using wetting films on a chip, *Opt. Express* 19 (2011) 17378–17389.
- [99] O. Mudanyali, E. McLeod, W. Luo, A. Greenbaum, A.F. Coskun, Y. Hennequin, C. P. Allier, A. Ozcan, Wide-field optical detection of nanoparticles using on-chip microscopy and self-assembled nanolenses, *Nat. Photonics* 7 (2013) 247–254.
- [100] E. McLeod, C. Nguyen, P. Huang, W. Luo, M. Veli, A. Ozcan, Tunable vapor-condensed nanolenses, *ACS Nano* 8 (2014) 7340–7349.
- [101] E. McLeod, T.U. Dincer, M. Veli, Y.N. Ertas, C. Nguyen, W. Luo, A. Greenbaum, A. Feizi, A. Ozcan, High-throughput and label-free single nanoparticle sizing based on time-resolved on-chip microscopy, *ACS Nano* 9 (2015) 3265–3273.
- [102] M.U. Dalgolu, A. Ray, Z. Gorocs, M. Xiong, R. Malik, G. Bitan, E. McLeod, A. Ozcan, Computational on-chip imaging of nanoparticles and biomolecules using ultraviolet light, *Sci. Rep.* 7 (2017) srep44157, <http://dx.doi.org/10.1038/srep44157>.
- [103] A. Ray, S. Li, T. Segura, A. Ozcan, High-throughput quantification of nanoparticle degradation using computational microscopy and its application to drug delivery nanocapsules, *ACS Photonics* 4 (2017) 1216–1224, <http://dx.doi.org/10.1021/acsp Photonics.7b00122>.
- [104] Z. Göröcs, E. McLeod, A. Ozcan, Enhanced light collection in fluorescence microscopy using self-assembled micro-reflectors, *Sci. Rep.* 5 (2015), <http://dx.doi.org/10.1038/srep10999>.
- [105] A. Wong, F. Kazemzadeh, C. Jin, X.Y. Wang, Bayesian-based aberration correction and numerical diffraction for improved lensfree on-chip microscopy of biological specimens, *Opt. Lett.* 40 (2015) 2233–2236, <http://dx.doi.org/10.1364/OL.40.002233>.
- [106] D. Loomis, Y. Grosse, B. Lauby-Secretan, F.E. Ghissassi, V. Bouvard, L. Benbrahim-Tallaa, N. Guha, R. Baan, H. Mattock, K. Straif, The carcinogenicity of outdoor air pollution, *Lancet Oncol.* 14 (2013) 1262–1263, [http://dx.doi.org/10.1016/S1470-2045\(13\)70487-X](http://dx.doi.org/10.1016/S1470-2045(13)70487-X).
- [107] g-metone, Model 804, Met One Instrum. (n.d.). <http://www.metone.com/products/indoor-particle-monitors/model-804/> (accessed March 10, 2017).
- [108] D. Harrison, R. Maggs, J. Booker, UK equivalence programme for monitoring of particulate matter, *Rep. Prod. Bur. Veritas Behalf Defra Devolved Adm. Rep. Ref. No BVAQAD202209DH2396*. (2006). <https://uk-air.defra.gov.uk/>

- assets/documents/reports/cat05/0606130952_UKPMEEquivalence.pdf (accessed November 13, 2016).
- [109] W.H. Walton, J.H. Vincent, Aerosol instrumentation in occupational hygiene: an historical perspective, *Aerosol Sci. Technol.* 28 (1998) 417–438.
- [110] Aerosol Instrumentation » Section 3, (n.d.). <http://aerosol.ees.ufl.edu/instrumentation/section03.html> (accessed May 28, 2016).
- [111] G. Mainelis, Collection of airborne microorganisms by electrostatic precipitation, *Aerosol Sci. Technol.* 30 (1999) 127–144, <http://dx.doi.org/10.1080/027868299304732>.
- [112] D. Broßell, S. Tröller, N. Dziurawitz, S. Plitzko, G. Linsel, C. Asbach, N. Azong-Wara, H. Fissan, A. Schmidt-Ott, A thermal precipitator for the deposition of airborne nanoparticles onto living cells—rationale and development, *J. Aerosol Sci.* 63 (2013) 75–86, <http://dx.doi.org/10.1016/j.jaerosci.2013.04.012>.
- [113] C. Liu, P.-C. Hsu, H.-W. Lee, M. Ye, G. Zheng, N. Liu, W. Li, Y. Cui, Transparent air filter for high-efficiency PM_{2.5} capture, *Nat. Commun.* 6 (2015) 6205, <http://dx.doi.org/10.1038/ncomms7205>.
- [114] J. Hirst, An automatic volumetric spore trap, *Ann. Appl. Biol.* 39 (1952) 257–265.
- [115] C.H. says, SCVNews.com | Sand Fire Grows to 3,327 Acres; 200-300 Evacuations | 07-22-2016, (n.d.). <http://scvnews.com/2016/07/22/sand-fire-grows-to-2500-acres-evacuations/> (accessed February 11, 2017).
- [116] N. Hudda, T. Gould, K. Hartin, T.V. Larson, S.A. Fruin, Emissions from an international airport increase particle number concentrations 4-fold at 10 km downwind, *Environ. Sci. Technol.* (2014). <http://pubs.acs.org/doi/abs/10.1021/es5001566> (accessed October 10, 2014).
- [117] E.J. Candès, T. Strohmer, V. Voroninski, PhaseLift: exact and stable signal recovery from magnitude measurements via convex programming, *Commun. Pure Appl. Math.* 66 (2013) 1241–1274, <http://dx.doi.org/10.1002/cpa.21432>.
- [118] E.J. Candès, X. Li, Solving quadratic equations via phaselift when there are about as many equations as unknowns, *Found. Comput. Math.* 14 (2014) 1017–1026, <http://dx.doi.org/10.1007/s10208-013-9162-z>.
- [119] F. Soulez, É. Thiébaud, A. Schutz, A. Ferrari, F. Courbin, M. Unser, Proximity operators for phase retrieval, *Appl. Opt.* 55 (2016) 7412–7421, <http://dx.doi.org/10.1364/AO.55.007412>.